Energy & Environmental Science

PAPER

View Article Online
View Journal | View Issue

Cite this: *Energy Environ. Sci.*, 2014, 7, 3371

An experimental and modeling/simulation-based evaluation of the efficiency and operational performance characteristics of an integrated, membrane-free, neutral pH solar-driven water-splitting system†

Jian Jin,*[ab] Karl Walczak,[b] Meenesh R. Singh,[bc] Chris Karp,[a] Nathan S. Lewis*[ad] and Chengxiang Xiang*[a]

The efficiency limits, gas-crossover behavior, formation of local pH gradients near the electrode surfaces, and safety characteristics have been evaluated experimentally as well as by use of multi-physics modeling and simulation methods for an integrated solar-driven water-splitting system that operates with bulk electrolyte solutions buffered at near-neutral pH. The integrated membrane-free system utilized a triple-junction amorphous hydrogenated Si (a-Si:H) cell as the light absorber, Pt and cobalt phosphate (Co–Pi) as electrocatalysts for the hydrogen-evolution reaction (HER) and oxygen-evolution reaction (OER), respectively, and a bulk aqueous solution buffered at pH = 9.2 by 1.0 M of boric acid/borate as an electrolyte. Although the solar-to-electrical efficiency of the stand-alone triple-junction a-Si:H photovoltaic cell was 7.7%, the solar-to-hydrogen (STH) conversion efficiency for the integrated membrane-free water-splitting system was limited under steady-state operation to 3.2%, and the formation of pH gradients near the electrode surfaces accounted for the largest voltage loss. The membrane-free system exhibited negligible product-recombination loss while operating at current densities near 3.0 mA cm^{-2}, but exhibited significant crossover of products (up to 40% H_2 in the O_2 chamber), indicating that the system was not intrinsically safe. A system that contained a membrane to minimize the gas crossover, but which was otherwise identical to the membrane-free system, yielded very low energy-conversion efficiencies at steady state, due to low transference numbers for protons across the membranes resulting in electrodialysis of the solution and the consequent formation of large concentration gradients of both protons and buffer counterions near the electrode surfaces. The modeling and simulation results showed that despite the addition of 1.0 M of buffering agent to the bulk of the solution, during operation significant pH gradients developed near the surfaces of the electrodes. Hence, although the bulk electrolyte was buffered to near-neutral pH, the electrode surfaces and electrocatalysts experienced local environments under steady-state operation that were either highly acidic or highly alkaline in nature, changing the chemical form of the electrocatalysts and exposing the electrodes to potentially corrosive local pH conditions. In addition to significant pH gradients, the STH conversion efficiency of both types of systems was limited by the mass transport of ionic species to the electrode surfaces. Even at operating current densities of <3 mA cm^{-2}, the voltage drops due to these pH gradients exceeded the combined electrocatalyst overpotentials for the hydrogen- and oxygen-evolution reactions at current densities of 10 mA cm^{-2}. Hence, such near-neutral pH solar-driven water-splitting systems were both fundamentally limited in efficiency and/or co-evolved explosive mixtures of H_2(g) and O_2(g) in the presence of active catalysts for the recombination of H_2(g) and O_2(g).

Received 16th June 2014
Accepted 24th July 2014

DOI: 10.1039/c4ee01824a

www.rsc.org/ees

[a]*Joint Center for Artificial Photosynthesis, California Institute of Technology, Pasadena CA 91125, USA. E-mail: jjin@lbl.gov; nslewis@caltech.edu; cxx@caltech.edu*

[b]*Engineering Division, Lawrence Berkeley National Laboratory, Berkeley CA 94720, USA*

[c]*Department of Chemical & Biomolecular Engineering, University of California Berkeley, CA 94720, USA*

[d]*Division of Chemistry and Chemical Engineering, California Institute of Technology, 210 Noyes Laboratory, 127-72, Pasadena, CA 91125, USA*

† Electronic supplementary information (ESI) available. See DOI: 10.1039/c4ee01824a

Broader context

Development of an integrated solar-driven water-splitting system has received increasing attention for large-scale solar energy-conversion and storage applications. To develop an efficient, scalable and safe technology, a cation-exchange membrane or an anion-exchange membrane is typically employed to separate the gaseous products and minimize the recombination losses in the system, as well as for other system design reasons. As a result, acidic or strong alkaline electrolytes are required to reduce the solution transport losses in the cell and to obtain high transference numbers for protons through the membrane. Alternatively, several studies have reported solar-driven water-splitting devices that operate in bulk electrolytes buffered to near-neutral pH in the absence of a membrane. However, the potential losses due to the pH gradient at the surface of the electrodes, and losses due to product crossover and recombination were not fully understood for those devices. To develop a stable, scalable and safe technology, these loss mechanisms and safety characteristics need to be critically addressed.

I. Introduction

Integrated photoelectrochemical systems comprised of semiconducting materials that capture and convert the energy from sunlight into separated charge carriers, catalysts that reduce the potential barrier for conversion of the charge carriers into fuels and oxygen, and membranes that conduct ions while enforcing the separation of chemical products, have been the subject of several design and optimization studies.[1–6] Obtaining new options for the light absorber, membrane, and electrocatalytic components that comprise the active device elements of a scalable solar-fuels system requires the innovative development of earth-abundant materials for such purposes.[7–16] However, challenges are also present in achieving efficient system-level operation. Important system-level considerations involve the minimization of any loss of electrical potential due to the resistance associated with ion transport in the electrolyte, as well as minimization of any loss of chemical potential due to crossover, mixing, and recombination of products, and safety concerns regarding the production of potentially explosive mixtures of H_2(g) and O_2(g) in the presence of active catalysts for recombination of the gases.[2,17,18] The ohmic losses can be minimized by ensuring adequate conductivity of the electrolyte and membrane, decreasing the ionic path length, and ensuring facile proton or hydroxide transport to minimize the pH gradients between the anode and cathode surfaces. Membranes or other porous materials can be used to separate the anodic and cathodic compartments of the system and thereby prevent deleterious product recombination and gas crossover. Hence, conventional electrolysis and photoelectrolysis system designs involve the use of acidic or alkaline electrolytes and/or a suitable cation- or anion-exchange membrane. Such systems also require a detailed analysis to obtain a suitable system geometry, as well as careful system construction to minimize the ionic path length and to enable the safe and efficient production of fuels.[2]

The requirements for materials stability would be considerably relaxed if an efficient solar-driven water-splitting system could operate robustly under near-neutral pH conditions. One challenge for a solar-driven water-splitting system operating at intermediate pH is the lack of membrane separators with high transference numbers for protons or hydroxide ions in these pH ranges. As a result, membrane-free systems, which necessarily result in co-evolved near-stoichiometric mixtures of H_2(g) and O_2(g) in the presence of active catalysts for H_2(g) and O_2(g) recombination, have been characteristic of almost all solar-driven water-splitting device demonstrations.[19–22] For example, an integrated device that contains a cobalt-based oxygen-evolution catalyst, a triple-junction amorphous hydrogenated Si (a-Si:H) photovoltaic cell, and a Ni–Mo–Zn hydrogen-evolution catalyst has been reported to exhibit a solar-to-hydrogen (STH) conversion efficiency, η_{STH}, of 2.5% during its limited lifetime of several hours of operation at near-neutral pH.[19] However, in a complete membrane-free solar-driven water-splitting system, the hydrogen produced at the cathode will cross over to the anode chamber either diffusively or convectively through the ionic conduction path, and will thus either produce hazardous gas mixtures in the reactor and/or increase the recombination rate of hydrogen oxidation at the anode, which will lower the overall system efficiency. Moreover, at operational conditions in near-neutral pH, significant pH gradients will develop near the surface of the electrodes. These concentration gradients will result in significant potential drops, degrading the efficiency of the system relative to the efficiency of the a-Si:H device alone.[23]

In this work, the efficiency limits, gas-crossover behavior, formation of local pH gradients near the electrode surfaces, and safety characteristics of complete systems have been evaluated experimentally for an integrated solar-driven water-splitting system that operates with bulk electrolyte solutions buffered at near-neutral pH. For this analysis, membrane-free and membrane-containing devices with identical semiconductor/catalyst assemblies were constructed to experimentally measure the overall efficiency as well as to determine the losses due to product crossover and recombination during steady-state operation of the system. To better understand the performance limits of the systems, simulations of the membrane-containing and membrane-free systems have also been performed using a multi-physics COMSOL model that accounts for the light absorption, carrier transport, catalytic reactions and electrochemical processes in the system, and that includes the potential losses associated with solution resistance and with the development of pH gradients near the electrodes.

II. Experimental methods and modeling approaches

A. Materials

Titanium (99.995%), nickel (99.995%), and molybdenum (99.95%) sputtering targets were obtained from Kurt J. Lesker, Livermore, CA. The platinum (99.99%) and iridium (99.9%) sputtering targets were obtained from Lawrence Berkeley National Laboratory.

The chemicals for catalyst deposition, electrochemical testing, and photoelectrochemical testing were acquired from Sigma Aldrich, St. Louis, MO. These chemicals included potassium phosphate monobasic (98%), cobalt(II) nitrate hexahydrate (99.999%), boric acid (98%), and potassium hydroxide (90%). H_2O with a resistivity of 18 MΩ cm was used throughout and was obtained from a Milli-Q Integral 3 purification system (Millipore, Billerica, MA 01821).

The chemicals for patterning the triple-junction a-Si:H cells were obtained from Gallade Chemical, Newark, CA. These chemicals included: potassium carbonate (90% purity), ammonium bifluoride (ACS reagent grade), nitric acid (ACS reagent grade), hydrochloric acid (ACS reagent grade), and iron chloride solution (ACS reagent grade).

B. Design of the solar-driven water-splitting device

Fig. 1a and b present cross-sectional schematic views of the membrane-containing and the membrane-free solar-driven water-splitting systems, respectively. The integrated photoelectrochemical (PEC) device, consisting of a light absorber and electrocatalysts, was mounted on a 22.5 mm × 22.5 mm acrylic frame that had a 22.5 mm × 5 mm slot on each side of the PEC assembly. To produce the membrane-containing system, the slot was covered by an ion-exchange membrane. The PEC device and the open slots were separated by a 1 mm × 0.5 mm thick portion of the acrylic frame. An acrylic window and a rubber gasket were used to seal each side of the PEC device. The complete cell had a ~5–7 mm thickness of electrolyte in each compartment, and was equipped with multiple inlet/outlet tubes (PEEK, 1.59 mm O.D and 0.75 mm I.D) for electrolyte filling and gas collection.

Fig. 1c shows a schematic illustration of an integrated membrane-free system equipped with an internally wired diagnostic device for monitoring the photocurrent density during the cell operation. An identical piece of the light absorber was employed, and the front surface was coated with an oxygen-evolution catalyst. However, the stainless-steel back contact was connected in series, through an external potentiostat (Biologic SP300) that served either as an ammeter or as a current source to drive the device at a particular reaction rate during the measurements, to a stainless-steel substrate that was coated with a hydrogen-evolution catalyst. The two stainless-steel pieces were then glued together using a thin layer of epoxy (Double/Bubble Epoxy, Royal Adhesives & Sealants, Wilmington, CA). The resulting assembly had the same physical dimensions as the fully integrated system (Fig. 1a and b) and allowed the direct measurement of the operating current for the device. Fig. 2a displays a photograph of an assembled system.

C. Preparation of triple-junction a-Si:H silicon samples

A sheet (23 cm × 33 cm) of triple-junction (3J) a-Si:H deposited on stainless steel was obtained from Xunlight or from Unisolar. From top to bottom, the 3J a-Si:H structure consisted of: (1) indium-doped tin oxide (ITO) that functioned as an electrical contact and a charge collector; (2) three monolithically connected photovoltaic cells, each consisting of a p–i–n stack of a-Si:H and a-Si:H alloyed with Ge, in which the top layer (absorbed blue), middle (absorbed green), and bottom (absorbed red) layers enabled enhanced absorption and utilization of light through the visible region of the solar spectrum; (3) zinc oxide (ZnO) and aluminum (Al), which reflected light back through the 3J a-Si:H; and (4) a stainless-steel substrate that served as the support structure for the device and also provided an electrical contact to the back side of the device. The sheet was etched into square pieces that had active light-absorbing areas of one of three different sizes: 19 mm × 19 mm; 16 mm × 16 mm; and 14 mm × 14 mm. The pieces were etched from the sheet using a combination of photolithography and chemical machining, because this process most reliably retained the original material specifications (~7 mA cm^{-2} short-circuit current density and 2.2 V open-circuit voltage) relative to other methods such as shearing, milling, water-jet cutting, and laser cutting.

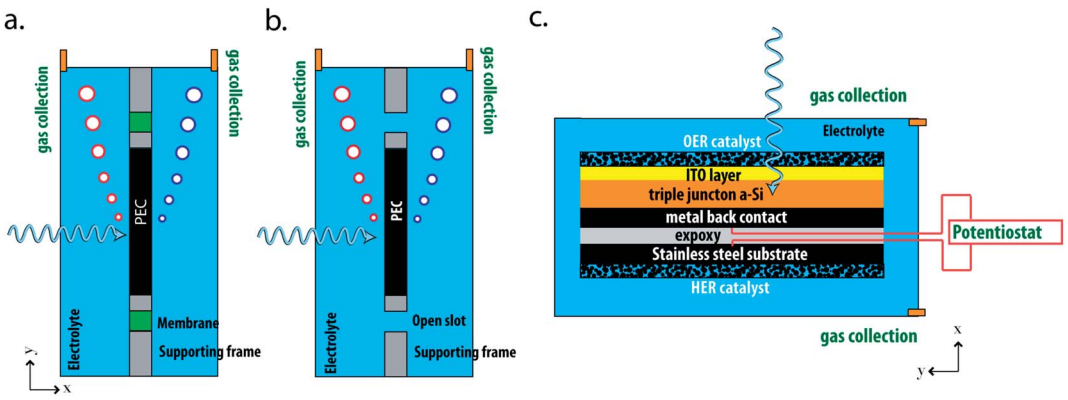

Fig. 1 Schematic illustrations of a device with a gas-impermeable ion-exchange membrane that enforces product separation (a) and of a membrane-free device (b). The black rectangles, labeled PEC, in (a) and (b) represent the light-absorbing materials coated with electrocatalysts, the green blocks represent cation-exchange membranes such as Nafion, and the grey rectangles represent acrylic supporting frames. (c) Schematic illustration of an integrated membrane-free device with an internally wired diagnostic device. Electrical contacts were made at the metal back contact and at the stainless steel substrates, where two copper wires were connected in series to a potentiostat. The metal back contact and the stainless steel substrate were glued together by a thin layer of epoxy.

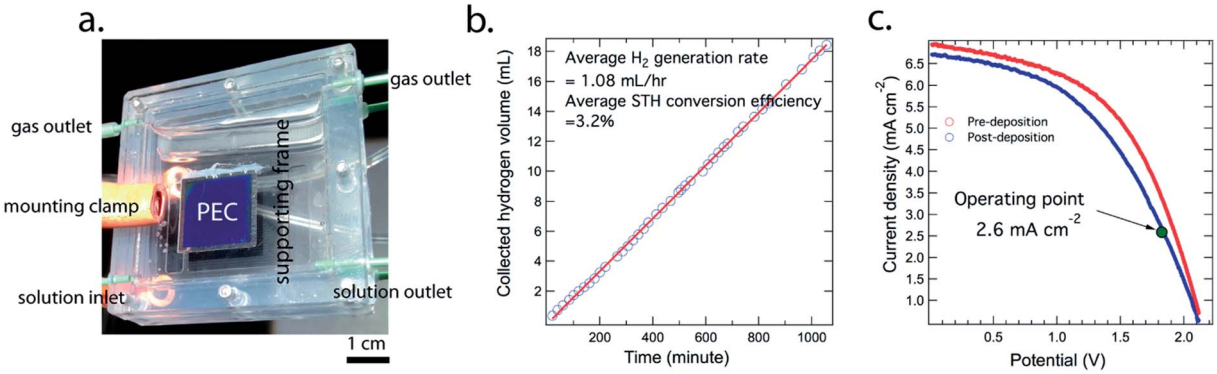

Fig. 2 (a) Photograph of an integrated, membrane-free solar-driven water-splitting device. (b) Rate of production of hydrogen gas in the cathode compartment. The average rate of H_2 production was calculated to be 1.08 mL h^{-1} from a linear fit of the experimental data. (c) Current–voltage characteristic of the triple-junction a-Si:H cell before and after catalyst deposition. The operating current density of the integrated device, 2.6 mA cm^{-2}, is indicated by a green circle.

Prior to photolithographic processing, the 3J a-Si:H sheet was rinsed with isopropanol and then dried under a stream of N_2(g). The ITO (top) side of the 3J a-Si:H was laminated with Riston MM115I photoresist using a Dupont Riston HRL hot-roll laminator (Dupont, Research Triangle Park, NC 27709) at 115 °C. The photoresist was then exposed to 50 mJ cm^{-2} of ultraviolet light, through a patterned mask, and was placed into a developer solution that consisted of 0.9 wt% ACS reagent-grade potassium carbonate (Gallade, Newark, CA, 94560, 90% purity) in distilled H_2O, to remove the unexposed portions of the photoresist. The unpatterned stainless-steel (bottom) side of the 3J a-Si:H sheet was then laminated with photoresist to protect the stainless steel during etching steps and to hold the pieces together during processing. The 3J a-Si:H sheet was then immersed for ~1 min in a bath containing 5 wt% ACS reagent-grade ammonium bifluoride (Gallade, Newark, CA, 94560) and 10 wt% ACS reagent-grade nitric acid (Gallade, Newark, CA, 94560) in distilled H_2O, until the exposed portions of the material changed color from blue to gray, indicating that the 3J a-Si:H had been removed from the substrate. The sheet was then immediately rinsed with H_2O. The zinc oxide and the aluminum back-reflector layers were then removed by immersing the sheet in a bath of 15 wt% ACS reagent-grade hydrochloric acid (Gallade, Newark, CA, 94560) in H_2O for ~2 min, until the exposed areas of the sheet turned from gray to shiny silver. The sheet was then removed from the bath and rinsed with H_2O. Another layer of photoresist was then applied on the top side over the existing layer of photoresist. The sheet was then exposed, and developed in an identical manner, but the pattern on the mask was 0.5 mm larger in all dimensions than the initial pattern. The sheet was subsequently immersed in an iron chloride solution (Gallade, Newark, CA, 94560) that contained 38.8 wt% iron(III) chloride and 0.2 wt% iron(II) chloride, and then in 0.18 wt% hydrochloric acid(aq.) for ~15 min, until the exposed areas of the stainless steel sheet had been completely removed. The sheet was then rinsed in H_2O. Finally, the photoresist on the back side of the stainless steel was removed by immersing the sheet in the developer solution.

D. Deposition of electrocatalysts

Two sets of 3J a-Si:H samples were fabricated: one set made use only of earth-abundant catalysts, and the other set made use of a noble-metal hydrogen-evolution catalyst and an earth-abundant oxygen-evolution catalyst. The earth-abundant catalysts used were Ni–Mo, for hydrogen evolution, and Co–Pi, for oxygen evolution, whereas Pt was used for the noble-metal hydrogen-evolution catalyst. An electrically driven electrolysis cell was also constructed with Pt- and iridium (Ir)-coated stainless-steel substrates as the cathode and anode, respectively.

Ni–Mo was incorporated into devices by radio-frequency (RF) co-sputtering of Ni and Mo onto the uncovered sides of the 3J a-Si:H pieces using an AJA 5-gun confocal sputtering system with a base pressure of 7×10^{-7} Torr. Prior to Ni–Mo deposition, the substrate was sputtered at 25 W for 3 min in an Ar plasma at 5 mTorr. To promote adhesion of the Ni–Mo, a 10 nm layer of titanium (99.995% pure) was deposited onto the substrate, at 3.7 W cm^{-2} at an Ar chamber pressure of 2 mTorr. The Ni (99.995% pure) and Mo (99.95% pure) were then co-sputtered in an Ar plasma at 2 mTorr chamber pressure, using power densities of 0.97 and 0.26 W cm^{-2}, respectively. The deposited Ni–Mo layer was 100 nm thick. All materials were sputtered at room temperature, and the deposition rates were determined using a quartz crystal thickness monitor.

Pt was deposited onto a-Si:H samples in a manner similar to that used for Ni–Mo. The samples underwent the same pre-deposition Ar-plasma etch, and a Ti adhesion layer was deposited prior to deposition of the Pt. Pt (99.99%) was deposited to a thickness of 100 nm using a power density of 3.7 W cm^{-2} at an Ar chamber pressure of 2 mTorr.

After the hydrogen-evolution catalysts had been applied to the exposed sides of the 3J a-Si:H pieces, the photoresist on the other side of the pieces was removed by soaking the pieces in 0.1 M KOH(aq.) for ~2 min until the photoresist lifted off. The pieces were then rinsed with H_2O and oxygen-evolution catalysts were then deposited onto the material.

Ir was deposited on stainless steel substrates that had the original 3J a-Si:H material completely etched away by either 1 M

H_2SO_4 or 1 M NaOH using a similar sputtering procedure to that used for Pt. The samples underwent the pre-deposition Ar-plasma etch, and a Ti adhesion layer was deposited prior to the deposition of Ir. Ir (99.99%) was deposited to a thickness of 75 nm using a power density of 3.7 W cm^{-2} and an Ar chamber pressure of 2 mTorr.

The Co–Pi oxygen-evolution catalyst was prepared following a published procedure,[24] and was applied using photodeposition. Briefly, a Co–Pi coating solution of 0.1 M potassium phosphate monobasic (Sigma Aldrich, 98%) and 0.5 mM cobalt(II) nitrate hexahydrate (Sigma Aldrich, 99.999%) was prepared in H_2O. A Co–KBi solution containing 1.0 M boric acid (Sigma Aldrich, 98%), 0.45 M KOH (Sigma Aldrich, 90%), and 0.25 mM of cobalt(II) nitrate hexahydrate (Sigma Aldrich, 99.999%) was prepared in H_2O. A potassium borate (KBi) solution was prepared and consisted of 1.0 M boric acid (Sigma Aldrich, 98%) and 0.45 M potassium hydroxide (Sigma Aldrich, 90%) in H_2O.

For "horizontal" deposition of Co–Pi, the 3J a-Si:H PEC chip was partially assembled into the system, with only the back window and gasket in place. The deposition was completed by filling the cell with the Co–Pi plating solution (Co–Kbi) and placing the cell for 5–60 min, depending on the desired film thickness, underneath a custom-made light source calibrated to ~100 mW cm^{-2}. For "vertical" deposition, the partially assembled system was filled with the Co–Pi coating solution and was irradiated for 30–90 min using an Oriel Sol3A class AAA solar simulator, equipped with an AM1.5 filter (Newport, Stratford, CT), with the light intensity set and calibrated to an irradiance of 100 mW cm^{-2}. Deposition of the Co–Pi catalyst in the vertical orientation caused the catalyst to accumulate along the edges of the 3J a-Si:H, due to gravity, because the Co compounds precipitated during the photoreaction. Rotating the system during the coating allowed a thick layer of Co–Pi to deposit along all of the edges, but was a much slower process than horizontal coating. Once the deposition was complete, the Co–KBi solution was drained and the materials assembly was rinsed with H_2O.

E. Cell operation and gas collection

The semiconductor/catalyst assembly was attached to the supporting frames in the system described above using epoxy (Double/Bubble Epoxy, Royal Adhesives & Sealants, Wilmington, CA). Both the cathode and the anode chambers were then filled with the buffered boric acid, KBi, solution (pH = 9.2). Two Tygon tubes, one connected to the anodic chamber and the other to the cathodic chamber, and each inserted into separate glass burettes filled with water, were used to measure the rates of production of gaseous products, because the bubbles were captured in the headspace of the burettes and pushed down the water level. Each tube was passed through a pinch valve, and the measurements of H_2 and O_2 production were alternated by releasing and then reclosing one tube at a time. The measured gas-production rates were converted to electrical currents by use of Faraday's law of electrolysis combined with the ideal gas law: 1 mA of electrical current is equivalent of 0.44 mL h^{-1} of H_2 generation (0.22 mL h^{-1} for O_2), at room temperature (25 °C). A small correction (typically 2–3%) was also applied to each data point to compensate for the pressure differential caused by the water level (typically 20–30 cm high) in each burette. The relationship between the current and the gas-production rate was verified experimentally using a water-splitting electrolyzer, and the calibration was performed regularly to confirm the continued accuracy of the relationship. The gas-production rates from the cathode and anode compartments generally maintained a ratio close to 2 : 1. The gas volumetric measurements used to determine the solar-to-hydrogen (STH) conversion efficiencies led to an estimated relative uncertainty of 10% in η_{STH}. To facilitate compositional analysis of the gaseous products by gas chromatography (GC), instead of the burettes, two small U-shaped glass tubes were used to collect the products. Each of the U-shaped tubes was filled with degassed H_2O and was sealed with a rubber septum at one end, to facilitate sampling of the gas by syringe as well as to allow for complete purging of the tube between measurements. A sufficient amount of gas for robust GC analysis was available every 20 min from the cathode compartment and every 40 min from the anode compartment. For each analysis, two gas-tight 125 μl syringes were used to draw 100 μl of gas into each syringe, and then 20 μl from each syringe was injected simultaneously into a two-channel GC analyzer (Agilent, 7890A Santa Clara, CA), one channel for H_2 and the other for O_2 and N_2.

F. Multiphysics modeling

The modeling of a fully integrated solar-driven water-splitting system primarily involves quantifying various efficiency losses in the device due to ohmic resistance drops, pH gradients, electrodialysis of the electrolyte, and crossover of the gaseous products. These losses result from concentration gradients that can develop for various species in the device, such as H^+, OH^-, K^+, $B(OH)_4^-$, $B(OH)_3$, H_2 and O_2.

The net molar flux of each species in the electrolyte, $\mathbf{N}_i$, is the sum of the fluxes due to migration, diffusion and convection, such that

$$\mathbf{N}_i = -D_i\nabla c_i - z_i u_i F c_i \nabla\phi_1 + \mathbf{v}c_i,\ i = 1,2,\ldots,n \quad (1)$$

where ϕ_1 is the electric potential, $\mathbf{v}$ is the velocity, c_i is the concentration, D_i is the diffusion coefficient, z_i is the charge number, $u_i = D_i/RT$ is the mobility where R is the ideal gas constant and T is the absolute temperature, and F is the Faraday constant. The conservation of mass requires that:

$$\frac{\partial c_i}{\partial t} + \nabla\cdot\mathbf{N}_i = R_i \quad (2)$$

where R_i is the net rate of formation of the i^{th} species due to bulk ionic reactions such as buffer and water-dissociation kinetics. The predominant source of convection in this system was due to product bubbles, which was neglected in the modeling. Electroneutrality was assumed at every point in the simulation space, such that

$$\sum_{i=1}^{n} z_i c_i = 0 \quad (3)$$

The current density in the liquid electrolyte, $\mathbf{i}_l$, was obtained from the total ionic flux,

$$\mathbf{i}_l = F\sum_{i=1}^{n} z_i \mathbf{N}_i \quad (4)$$

The charge-transfer kinetics at the electrodes were represented according to the Butler–Volmer model as:

$$-\mathbf{n}\cdot\mathbf{i}_s = \mathbf{n}\cdot\mathbf{i}_l = i_R = i_0\left[e^{\frac{\alpha_a F(\phi_s-\phi_l-E_0)}{RT}} - e^{-\frac{\alpha_c F(\phi_s-\phi_l-E_0)}{RT}}\right] \quad (5)$$

where E_0 is the equilibrium potential, i_0 is the exchange-current density and α_a and α_c are anodic and cathodic transfer coefficients. All other boundaries in the system were modeled as being fully insulated. The current flow in the metallic solid, $\mathbf{i}_s$, is governed by Ohm's law,

$$\mathbf{i}_s = -\sigma_s \nabla\phi_s \quad (6)$$

where σ_s is the conductivity of the solid. Eqn (7) resulted as a consequence of electroneutrality:

$$\nabla\cdot\mathbf{i}_l = -\nabla\cdot\mathbf{i}_s = 0 \quad (7)$$

To simulate η_{STH} of the integrated system, the experimentally obtained current–voltage characteristic for the light-absorbing component was employed as the boundary condition at the photoelectrode. The operating current densities measured using the internally wired devices were employed as a Neumann (or second-type) boundary condition for the current flux at the photoelectrode.

III. Results

A. Membrane-free device

a. STH conversion efficiency. Fig. 2b shows measurements of the amount of hydrogen gas formed in the cathode chamber during operation of the membrane-free system. The average rate of hydrogen production was 1.08 mL h^{-1}, which corresponded to the operating current density of 2.6 mA cm^{-2} and a STH conversion efficiency, η_{STH}, of 3.2%. The performance of the integrated system was also investigated using different photodeposition methods for the Co–Pi oxygen-evolution catalyst. Similar STH conversion efficiencies were observed with various deposition techniques (see ESI†). Fig. 2c shows the current–voltage characteristic of the 3J a-Si:H cell before and after the deposition of the electrocatalysts. Although the open-circuit voltage exhibited minimal change after the catalyst deposition, the short-circuit current density decreased from 7.0 mA cm^{-2} to 6.7 mA cm^{-2} after deposition, due to obstruction of the incident light by the catalysts. However, in the fully operational membrane-free solar-driven water-splitting system, the operating current density for the device was only 2.6 mA cm^{-2}, as indicated by a green circle in the plot.

To more fully understand this behavior, the performance of the integrated membrane-free system was simulated by a multiphysics model that accounted for the electronic and ionic transport in the system. Fig. 3a shows the simulated current density as a function of the normalized distance, l/l_0, where l_0 is the total length of the electrode (16 mm) and l is the distance from the edge of the electrode. The average current density was calculated to be 2.5 mA cm^{-2} by integrating the current density along the width of the electrode, and η_{STH} was determined to be 3.1%. Both simulated results were therefore in excellent agreement with the experimental data on the fully operational system.

One of the potential losses in the system results from the pH gradient that develops near the surfaces of the electrodes. Fig. 3b shows the calculated pH profile for the system. Although the electrolyte was strongly buffered to pH = 9.2 with 1.0 M boric acid/borate, during operation even at 2.5 mA cm^{-2} of current density, the pH at the surface of the photocathode varied from 13.3 to 13.5, and the pH at the surface of the photoanode varied from 6.4 to 7.0. The average voltage loss due to the pH gradient was 400 mV. For comparison, the catalytic overpotentials for the Co–Pi oxygen-evolution and Pt hydrogen-evolution reactions in this same electrolyte, as determined using conventional three-electrode potentiostatic techniques, were 370 mV and 11 mV, respectively.

Assuming no convective mixing during operation, the simulation yielded a limiting current density of 2.8 mA cm^{-2} in this system due to mass-transport limitations of the buffered electrolyte in the cell. Because the potential loss due to the pH gradient and mass transport follows a sigmoid relationship as a function of the operational current density, and because the operational current density, 2.5 mA cm^{-2}, is close to the mass-transport-limited current density, an improvement of the photoabsorber and electrocatalyst performance would not result in the same percentage of increase in the overall system performance. In fact, minimal increase in the cell efficiency in this system is expected under such circumstances, because the additional voltage provided by a superior semiconductor/catalyst system would instead primarily drop across the electrolyte solution.

b. Losses due to recombination of products. One of the major concerns regarding operation of a solar-driven water-splitting system that does not contain a mechanism to separate the gaseous products is the efficiency loss that results from recombination of products due to gas crossover. When the potentiostat in the internally wired system was employed as an ammeter, the measured average current density on that specific 3J a-Si:H device was 1.5 ± 0.1 mA cm^{-2}, as compared to a current density of 1.54 ± 0.1 mA cm^{-2} calculated from the rate of hydrogen production in the same system. Chronoamperometry was also performed using the potentiostat to drive the internally wired a-Si:H device (Co–Pi for OER and Pt for HER) at current densities of 1.5, 3.0 or 5.0 mA cm^{-2}, respectively, under illumination. The applied voltages that were needed to produce these current densities were 30 mV, 330 mV and 1000 mV, respectively. In this configuration, the system could be tested while producing much higher or lower current densities than a wireless device could provide due to the limitations on the latter imposed by the voltage drops present in the solution under steady-state conditions. The corresponding

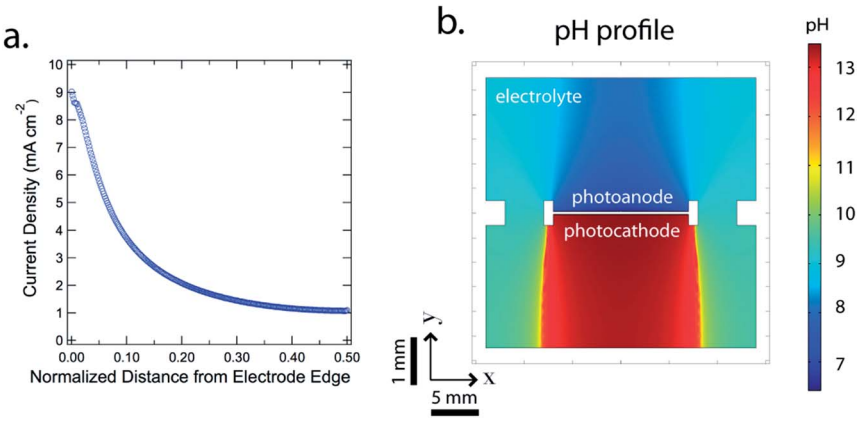

Fig. 3 (a) Current density as a function of the normalized distance from the photoelectrode edge from the simulation, (b) cross-sectional pH profiles in the membrane-free device from the COMSOL Multiphysics simulation.

current densities calculated based on the collection of the gaseous products were 1.49, 2.98 and 4.67 ± 0.1 mA cm^{-2}, respectively. The same level of agreement between the current density applied by the potentiostat and the implied current density based on the hydrogen-production rate was observed for a wired electrolysis device that had Ir at the anode and Pt at the cathode. Although a larger recombination loss (~6.6%) was observed during operation at the highest current density used in the experiment, the internally wired, membrane-free device exhibited low recombination losses (<5%) at operating current densities of 1.5 and 3.0 mA cm^{-2}.

c. Crossover of product gases. The crossover of gaseous products is another major concern for a membrane-free solar-driven water-splitting device. Fig. 4 shows the time evolution of the gas compositions in the cathode and anode chambers of the membrane-free device as determined by GC measurements. Over 2.5 h of operation, in the cathode compartment H_2 increased from 70 vol% to 80 vol%, O_2 increased from 5 vol% to 10 vol%, and air decreased from 25 vol% to 12 vol%. Over 2.5 h of operation, in the anode compartment H_2 increased from 20 vol% to 35–40 vol%, O_2 remained at 50–60 vol% and air decreased from 25 vol% to 12 vol%. The gradual change of the air composition from 25 vol% to 12 vol% was due to the degassing of the electrolyte and the value reached steady state in 2.5 h. The remaining 12 vol% air after 2.5 h resulted from outgassing from the interior wall surfaces of the generator (9 vol%) and the GC baseline from the analysis procedure (3 vol%) (see ESI, Table S1†). In the membrane-free device, 10 vol% O_2(g) was measured in the cathode chamber, while up to 40 vol% H_2(g) was measured in the anode chamber. Because the total gas-production rate of the cathode with respect to the anode was close to 2 : 1, the results indicated that 20 vol% of the total H_2 generated in the cathode compartment crossed over to the anode compartment, while 20 vol% of the total O_2 generated in the anode compartment crossed over to the cathode compartment. A flammable and potentially explosive gas mixture was therefore produced in both chambers of the system. The mutual similarity of these two crossover rates suggests that the gas crossovers resulted from diffusion and evaporation of dissolved product molecules.

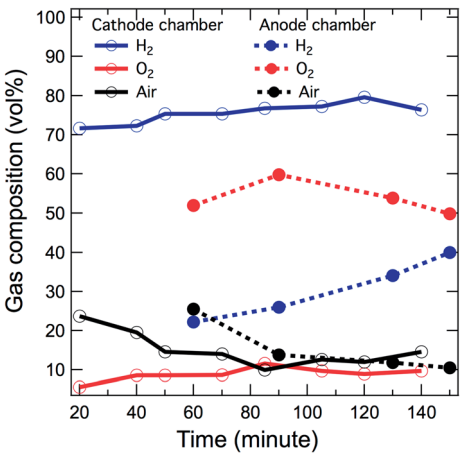

Fig. 4 Time evolution of the gas composition (H_2, O_2 and air) in the cathode compartment (solid lines) and the anode compartment (dashed lines).

B. Membrane-based system

Relative to the behavior of the membrane-free system with the same buffered pH (pH = 9.2) of the bulk electrolyte solution, introduction of a membrane into the system significantly reduced the rate of gas generation, and also produced a significant reduction in the operating current density. At steady state, η_{STH} was estimated to be <0.1% for the membrane-containing system, with the exact value uncertain due to experimental difficulties related to collection of the gaseous products at the observed very low rate of product-gas generation. As expected, the system eventually ceased to operate due to depletion of potassium ions in the anode compartment. However, imperfectly sealed systems (with a few pin-holes or cracks along the sealing edges of the photoelectrodes or membranes) operated continuously for many hours, and exhibited a value of η_{STH} that ranged from 0.1% to 0.5%.

IV. Discussion

A. Solar-driven water-splitting system at intermediate pHs

The membrane-free system based on the 3J a-Si:H photoactive device exhibited $\eta_{STH} = 3.2\%$, which is higher than the $\eta_{STH} = 2.5\%$ that has been reported previously for a comparable device structure,[19] due to the improved semiconductor processing and catalyst deposition protocols described herein. Nevertheless, product-gas crossovers caused the composition of gases in both the anode and cathode compartments to significantly exceed the flammability limit (4 vol%), due to the lack of a membrane separator. Hence, regardless of the value of η_{STH}, the implementation and deployment of such a system as a large-scale, manufacturable, solar-fuels technology would be exceedingly problematic. Many reported "high" efficiency values for photochemical devices[19–22] are therefore not representative of the actual η_{STH} values obtainable for complete, robust, intrinsically safe, practically deployable, solar-driven water-splitting systems.

The voltage penalty (400 mV at 3 mA cm^{-2} of current density) associated with operation at near-neutral pH in the bulk buffered electrolyte solution was the largest source of electric or chemical potential loss in this study. This voltage loss was larger than the voltage loss due to the HER and OER catalytic overpotentials combined. As a result, the operating current density of the full system, indicated in Fig. 2c, was significantly lower than the operating current density expected based upon the performance characteristics for the photoabsorber and the catalyst system, in which $\eta_{STH} > 6\%$ could in principle have been achieved if the pH at the surface of the electrode had matched the pH of the bulk electrolyte. However, η_{STH} for the actual system was limited to <4%, due to the pH gradient that developed, as well as due to mass-transport limitations.

Use of the wired device structure showed that an additional 1 V of applied voltage was required to produce an increase in the current density from 1.5 mA cm^{-2} to 5.0 mA cm^{-2} in the system under consideration. This behavior is expected because operation at current densities (2.5 mA cm^{-2}) near the mass-transport-limited current density (2.8 mA cm^{-2}) requires significant increases in the photovoltage to overcome the associated increased voltage drop in the electrolyte. Although the overpotentials exhibited by the Co–Pi electrocatalyst are >400 mV at current densities of 10 mA cm^{-2}, and thus exceed significantly the overpotentials for highly active OER catalysts under either neutral, acidic, or alkaline conditions,[8,25] these system-level considerations indicate that relatively little improvement in the system efficiency would be obtained by further reduction in the OER electrocatalyst overpotentials under these system operating conditions. Further increases in the limiting current density could be achieved by bubble evolution and/or by active stirring, however convective transport of the electrolyte in the cell is likely to increase the product gas crossover in the membrane-free device.

Even though the bulk electrolyte was buffered at near-neutral pH = 9.2, under operation of the system even at moderately low current densities (3 mA cm^{-2}), the local pH values near the electrodes were driven significantly towards alkaline or acidic conditions at steady state, due to the consumption of protons at the cathode and the liberation of protons at the anode of the water-splitting system. Hence, evaluation of the properties of the individual electrocatalysts in three-electrode potentiostatic experiments in well-stirred near-neutral pH buffered electrolytes does not capture the actual local pH near either the anode or the cathode during steady-state operation of a full solar-driven water-splitting system, with or without the presence of a membrane. The pH gradients would be more severe in the absence of buffer or at higher current densities, providing a self-limiting barrier to obtaining significant improvements in the efficiency of such a system regardless of the performance of the light-absorbers or electrocatalysts under system operational conditions.

B. Comparison between the membrane-based system and the membrane-free system

Significant differences in the extent of product crossover were observed between the membrane-based and membrane-free systems. Significant product crossover, with as much as 20% of the total H_2 gas produced found in the anode compartment, was observed in the membrane-free system, although no significant convective flow was observed during the study. The same measurements for product crossover could not be performed in the corresponding membrane-based system because the steady-state cell efficiency was limited to <0.1% under operation at near-neutral pH (pH = 9.2). To validate the product separation in a membrane-based system, a custom-built electrolyzer unit, which contained two Pt mesh electrodes separated by an anion-exchange membrane or cation-exchange membrane for OER and HER, was constructed. When the electrolyzer unit was operated at 10 mA cm^{-2} by a potentiostat in a strong acid, base or near-neutral electrolyte, minimal recombination loss (<5%) and product crossover (<5%) were observed, as expected.

The presence of the membrane further increased the pH gradients that developed in the system during operation in sunlight. The cation-exchange membrane, *i.e.*, Nafion, cannot support sufficient transport of protons between the cathode and anode compartments in intermediate pH solutions at steady state. As a result, the pH at the surface of the cathode and anode electrodes changed significantly from their initial bulk pH values. As the pH of the electrolyte increased at the cathode and decreased at the anode, an additional voltage (59 mV per pH unit) was required to drive the entire reaction, as predicted from the Nernst equation. Thus, η_{STH} was <0.1% for the membrane-based system. The numerical model predicted[23] the same transient decay as well as the low steady-state current densities observed for the membrane-containing system evaluated in this study. Removal of the cation-exchange membrane allowed buffer anions and neutral species to migrate/diffuse between the two compartments and thus partially alleviated, but did not fully eliminate, the pH gradient that developed during system operation, albeit at the expense of not facilitating an effective separation of the product gases.

Modeling and simulation of a membrane-based system that operates in either strong base or strong acid (*i.e.*, 1 M KOH or

1 M H_2SO_4) has revealed a range of geometric dimensions of a solar-driven water-splitting system[1,2] for which η_{STH} is not limited by the device architecture. This behavior is in accord with characteristics of conventional membrane-based electrolyzers and fuel cells that operate in acidic or alkaline media. The dimensions of the cell employed in this study were within the optimal cell dimensions indicated by such prior modeling and simulations[1,2] and would therefore result in minimal resistive loss and negligible pH gradients at the electrode surfaces during operation under such conditions. Based on the performance characteristics of the materials assembly (the triple junction a-Si:H as the light absorber, Pt and Co–Pi as the electrocatalysts for HER and OER), the numerical modeling indicated that the corresponding η_{STH} is expected to be >5% for a device that is operated under such conditions. However, the materials assembly investigated herein rapidly corroded in contact with either strong base or strong acid.

A geometry in which the photoelectrodes contained a series of small holes separated by a distance comparable to the thickness of the device (*i.e.* by a few micrometers) would alleviate some of the transport issues presented by the membrane-free device and would indeed lower, but not eliminate, the pH gradient. However, the introduction of small holes would result in a significant increase in the rates of diffusive and convective product crossover. Moreover the "hole-structure" architecture is not well-suited for use in a membrane-based system due to the low transference numbers of the buffer ions in the membrane.

C. Convective transport due to bubble formation

The numerical modeling and simulation of pH profiles and product-gas crossovers assumed that no convective force was present during system operation, and that the ionic species and gaseous products in the solution were transported by diffusion and/or migration. However, during the experimental measurements, small convective forces due to the formation and evolution of hydrogen and oxygen bubbles facilitated mass transport in both compartments. Although increased convective flux in the system facilitates mass transport, increases in convection also result in increased crossover of products. The modeling and simulation showed that if diffusive transport were the only driving force for the product-gas crossovers, then this particular membrane-free system geometry would result in only 0.2% crossover. However, product crossover as high as 20% was observed experimentally. The movement of the electrolyte, which is saturated with O_2 on one side and H_2 on the other, by convective forces allows movement of the products to the opposite compartment, and is likely to be the main driving force for the product-gas crossovers (see ESI† for more detailed discussion). Note that in a deployed full solar-driven water-splitting system, a pressure differential is required in the collection piping to facilitate beneficial collection of the H_2(g) product gas, but the 2 : 1 stoichiometry of H_2(g) to O_2(g) associated with water splitting will necessitate extremely precise control of the pressure differentials (which are expected to vary significantly in both space and time in a solar-driven water-splitting system) to avoid significant convective flow of the electrolyte during sustained operation of the membrane-free system.

D. Electrode-specific system operational constraints

The issues described and discussed above are general to any photoelectrochemical system operating at the specified interfacial fluxes in the electrolytes and system geometry under consideration. Hence, the same constraints would apply to dye-sensitized molecular photoelectrode systems, to molecular photosensitizers coupled to colloidal or molecular fuel-forming catalysts, and/or to other functional systems that produced the same solar-driven water-splitting fluxes at the boundary surface of the electrode/electrolyte interface as those considered herein both experimentally and in the modeling/simulation efforts.

The 3J a-Si:H with Ni–Mo and Co–Pi earth-abundant electrocatalysts exhibited other features that affected its potential for operation as an efficient, robust solar-fuels generation system. Specifically, use of sea water as an electrolyte would result in the cathodic deposition of metal impurities onto the cathode of the system, thereby poisoning the cathode for the HER, even if the performance of the anode were unaffected by the chemical impurities in the feed solution and/or in the standing electrolyte. Additionally, the specific 3J a-Si:H system with Ni–Mo and Co–Pi HER and OER electrocatalysts, respectively, was observed to be unstable upon immersion in the dark in buffered or unbuffered sea water. After 24 h of immersion in sea water in the dark, the photoactive film debonded from the stainless-steel substrate, presumably due to corrosion induced by the high chloride concentration of sea water. Additionally, under operating conditions, the equilibrium between Co species in the OER film on the anode and soluble Co species in the electrolyte solution will result in dissolution and also would facilitate the deposition of Co at the cathode, eventually leaching much of the Co electrocatalyst from the anode surface and limiting the duration of the membrane-free system operation at the ~3% STH efficiencies observed herein.

V. Conclusions

A fully integrated membrane-free solar-driven water-splitting system with a solar-to-hydrogen conversion efficiency of 3.2% was demonstrated, and the behavior of this system was compared experimentally and using multi-physics modeling to that of an identical system that additionally incorporated an ion-exchange membrane. The integrated system contained a triple junction a-Si:H light absorber, Pt and Co–Pi as the electrocatalysts for HER and OER, respectively, and operated in an intermediate pH bulk electrolyte that was strongly buffered by use of a 1.0 M boric acid/borate buffer (pH = 9.2). The observed photocurrent showed excellent agreement with the observed rate of hydrogen production and indicated minimal recombination loss from oxygen reduction at the cathode and hydrogen oxidation at anode. Analysis of the gas composition in the cathode and anode compartments showed high product-gas crossover, with 10% O_2(g) found in the cathode chamber and up to 40% H_2(g) measured in the anode chamber. Hence this

system was not intrinsically safe, and constituted a significant explosion hazard during operation, producing flammable mixtures of H_2(g) and O_2(g) in the presence of active catalysts (as well as in the presence of heat and light) for the recombination of H_2(g) and O_2(g).

The value of η_{STH} calculated using the multiphysics numerical simulation showed excellent agreement with the experimental results. The modeling showed that the largest efficiency loss in the system resulted from the concentration overpotential due to the pH gradient that developed at the electrode surfaces. Hence even though the bulk electrolyte was buffered at near-neutral pH = 9.2, under operation of the system even at moderately low current densities (3 mA cm^{-2}), the local pH values near the electrodes were driven significantly towards alkaline or acidic conditions at steady state due to the consumption of protons at the cathode and the liberation of protons at the anode of the water-splitting system. Operating at 2.5 mA cm^{-2}, the average potential loss due to the pH gradient in the system was 400 mV, whereas the overpotential for the hydrogen-evolution and oxygen-evolution reactions were 370 mV and 11 mV, respectively. Use of a near-neutral buffered pH electrolyte therefore produced larger overpotentials due to the resulting pH gradients than the kinetic overpotentials associated with the reasonably active electrocatalysts for the water splitting reaction itself. Further improvements to the performance of the light absorber or the catalyst materials would only result in small changes in the overall STH conversion efficiency, due to mass transport limitations of species to the electrodes, for a system that operates with the bulk electrolyte buffered to near-neutral pH values.

Acknowledgements

This material is based upon work performed by the Joint Center for Artificial Photosynthesis, a DOE Energy Innovation Hub, supported through the Office of Science of the U.S. Department of Energy under Award Number DE-SC0004993.

References

1 S. Haussener, S. Hu, C. Xiang, A. Z. Weber and N. Lewis, *Energy Environ. Sci.*, 2013, **6**, 3605–3618.
2 S. Haussener, C. X. Xiang, J. M. Spurgeon, S. Ardo, N. S. Lewis and A. Z. Weber, *Energy Environ. Sci.*, 2012, **5**, 9922–9935.
3 S. Hu, C. X. Xiang, S. Haussener, A. D. Berger and N. S. Lewis, *Energy Environ. Sci.*, 2013, **6**, 2984–2993.
4 L. C. Seitz, Z. B. Chen, A. J. Forman, B. A. Pinaud, J. D. Benck and T. F. Jaramillo, *ChemSusChem*, 2014, **7**, 1372–1385.
5 C. Xiang, Y. Chen and N. S. Lewis, *Energy Environ. Sci.*, 2013, **6**, 3713–3721.
6 Y. K. Chen, C. X. Xiang, S. Hu and N. S. Lewis, *J. Electrochem. Soc.*, 2014, **161**(10), 1101–1110.
7 J. R. McKone, N. S. Lewis and H. B. Gray, *Chem. Mater.*, 2014, **26**, 407–414.
8 M. G. Walter, E. L. Warren, J. R. McKone, S. W. Boettcher, Q. X. Mi, E. A. Santori and N. S. Lewis, *Chem. Rev.*, 2010, **110**, 6446–6473.
9 N. S. Lewis and D. G. Nocera, *Proc. Natl. Acad. Sci. U. S. A.*, 2007, **104**, 20142.
10 C. C. L. McCrory, S. Jung, J. C. Peters and T. F. Jaramillo, *J. Am. Chem. Soc.*, 2013, **135**, 16977–16987.
11 T. R. Cook, D. K. Dogutan, S. Y. Reece, Y. Surendranath, T. S. Teets and D. G. Nocera, *Chem. Rev.*, 2010, **110**, 6474–6502.
12 J. Suntivich, K. J. May, H. A. Gasteiger, J. B. Goodenough and Y. Shao-Horn, *Science*, 2011, **334**, 1383–1385.
13 Q. X. Mi, Y. Ping, Y. Li, B. F. Cao, B. S. Brunschwig, P. G. Khalifah, G. A. Galli, H. B. Gray and N. S. Lewis, *J. Am. Chem. Soc.*, 2012, **134**, 18318–18324.
14 M. Long, W. M. Cai, J. Cai, B. X. Zhou, X. Y. Chai and Y. H. Wu, *J. Phys. Chem. B*, 2006, **110**, 20211–20216.
15 A. Kudo, K. Omori and H. Kato, *J. Am. Chem. Soc.*, 1999, **121**, 11459–11467.
16 A. Kay, I. Cesar and M. Gratzel, *J. Am. Chem. Soc.*, 2006, **128**, 15714–15721.
17 E. A. Hernandez-Pagan, N. M. Vargas-Barbosa, T. H. Wang, Y. X. Zhao, E. S. Smotkin and T. E. Mallouk, *Energy Environ. Sci.*, 2012, **5**, 7582–7589.
18 J. Newman and K. Thomas-Alyea, *Electrochemical Systems*, Wiley & Sons, 2004.
19 S. Y. Reece, J. A. Hamel, K. Sung, T. D. Jarvi, A. J. Esswein, J. J. H. Pijpers and D. G. Nocera, *Science*, 2011, **334**, 645–648.
20 O. Khaselev and J. A. Turner, *Science*, 1998, **280**, 425–427.
21 S. Licht, B. Wang, S. Mukerji, T. Soga, M. Umeno and H. Tributsch, *J. Phys. Chem. B*, 2000, **104**, 8920–8924.
22 R. E. Rocheleau, E. L. Miller and A. Misra, *Energy Fuel*, 1998, **12**, 3–10.
23 M. R. Singh, C. Xiang and N. S. Lewis, 2014, manuscript in preparation.
24 M. W. Kanan and D. G. Nocera, *Science*, 2008, **321**, 1072–1075.
25 C. C. L. McCrory, S. H. Jung, J. C. Peters and T. F. Jaramillo, *J. Am. Chem. Soc.*, 2013, **135**, 16977–16987.

